

Formation of wind-captured disks in supergiant X-ray binaries

Consequences for Vela X-1 and Cygnus X-1

I. El Mellah¹, A. A. C. Sander^{2,3}, J. O. Sundqvist⁴, and R. Keppens¹

¹ Centre for mathematical Plasma Astrophysics, Department of Mathematics, KU Leuven, Celestijnenlaan 200B, 3001 Leuven, Belgium
e-mail: ileyk.elmellah@kuleuven.be

² Armagh Observatory and Planetarium, College Hill, Armagh BT61 9DG, UK

³ Institut für Physik und Astronomie, Universität Potsdam, Karl-Liebknecht-Str. 24/25, 14476 Potsdam, Germany

⁴ KU Leuven, Instituut voor Sterrenkunde, Celestijnenlaan 200D, 3001 Leuven, Belgium

Received 23 October 2018 / Accepted 5 January 2019

ABSTRACT

Context. In supergiant X-ray binaries (SgXB), a compact object captures a fraction of the wind of an O/B supergiant on a close orbit. Proxies exist to evaluate the efficiency of mass and angular momentum accretion, but they depend so dramatically on the wind speed that given the current uncertainties, they only set loose constraints. Furthermore, these proxies often bypass the impact of orbital and shock effects on the flow structure.

Aims. We study the wind dynamics and angular momentum gained as the flow is accreted. We identify the conditions for the formation of a disk-like structure around the accretor and the observational consequences for SgXB.

Methods. We used recent results on the wind launching mechanism to compute 3D streamlines, accounting for the gravitational and X-ray ionizing influence of the compact companion on the wind. Once the flow enters the Roche lobe of the accretor, we solved the hydrodynamics equations with cooling.

Results. A shocked region forms around the accretor as the flow is beamed. For wind speeds on the order of the orbital speed, the shock is highly asymmetric compared to the axisymmetric bow shock obtained for a purely planar homogeneous flow. With net radiative cooling, the flow always circularizes for sufficiently low wind speeds.

Conclusions. Although the donor star does not fill its Roche lobe, the wind can be significantly beamed and bent by the orbital effects. The net angular momentum of the accreted flow is then sufficient to form a persistent disk-like structure. This mechanism could explain the proposed limited outer extension of the accretion disk in Cygnus X-1 and suggests the presence of a disk at the outer rim of the neutron star magnetosphere in Vela X-1 and has dramatic consequences on the spinning up of the accretor.

Key words. accretion, accretion disks – X-rays: binaries – stars: black holes – stars: neutron – supergiants – stars: winds, outflows

1. Introduction

Most stars are found in multiple stellar systems, especially the high mass stars (Duchêne & Kraus 2013). Among these stars, a significant percentage undergo a phase of mass transfer that can seriously alter their subsequent evolution (Sana et al. 2012). New observational insights on the long- (Abbott et al. 2016) and short-term (Grinberg et al. 2017) evolution of high mass X-ray binaries (HMXB) have resulted in a compelling need for a more comprehensive description of mass transfer via wind accretion.

In supergiant X-ray binaries (SgXB), a supergiant O/B donor star is orbited by a compact object, often a neutron star (NS) embedded in the stellar wind (for a recent review, see Martínez-Núñez et al. 2017). O/B stars are known to lose mass at a rate up to several $10^{-6} M_{\odot} \text{yr}^{-1}$ through a wind whose launching mechanism was first analyzed in detail by Lucy & Solomon (1970) and Castor et al. (1975): the resonant line absorption and scattering of UV photons by partly ionized metal ions provides the outer layers of the star with a net outward momentum. As the flow accelerates, it keeps absorbing previously untouched Doppler-shifted line photons and eventually reaches terminal speeds up to 2000 km s^{-1} . The gravitational capture of a fraction of this abundant line-driven wind by the compact companion produces the X-ray luminosity, on the order

of $10^{35-37} \text{ erg s}^{-1}$, that we observe in SgXB (Walter et al. 2015; Martínez-Núñez et al. 2017 and Fürst et al. 2018).

Until now, the mass and angular momentum accretion rates pertaining wind accretion have been evaluated based on the Bondi-Hoyle-Lyttleton model (BHL; see Edgar 2004, for a review). In this model, a planar supersonic flow is gravitationally deflected by the gravitational field of a point mass and an overdense tail is formed in its wake. The mass accretion rate turns out to be extremely sensitive to the relative speed of the flow with respect to the accretor. In SgXB, the terminal wind speed is generally measured within $\sim 20\%$ but the accretor lies very close from the stellar surface, in a region where the wind is still accelerating and where orbital effects may significantly alter the picture of a purely radial wind; the theoretical uncertainty on the magnitude and orientation of the wind velocity field within the orbital separation makes the sharp dependency of the BHL mass accretion rate on the wind speed even more crippling. Furthermore, the axisymmetry of the BHL problem has circumvented any discussion of the accretion of angular momentum. This assumption was first relaxed by Illarionov & Sunyaev (1975) and Shapiro & Lightman (1976) to assess the possibility of the formation of a wind-captured disk around compact accretors. These authors concluded that it was likelier for close binaries, where the star gets close to fill its Roche lobe, but

that it was, once again, highly dependent on the relative wind speed. More recently, wind-captured disks have also been identified in simulation of black holes accreting matter from a smooth wind (Walder et al. 2013). Once we complement the models by accounting for the inhomogeneities known to form in this type of winds (Sundqvist et al. 2018), any realistic SgXB-ray accretion luminosity can be reproduced if we rely only on the BHL formula. The question of wind-captured disks also received renewed interest in light of recent results on planetary and pre-planetary nebulae that predominantly exhibit aspherical structure. Most of these are now thought to be the result of binary interaction (De Marco 2009; Jones & Boffin 2017). The orbital motion induced by binarity can lead to density enhancements in the orbital plane (see, e.g., Decin et al. 2019, for the impact on the measured mass loss rates of asymptotic giant branch stars), while disk-driven jets shape the circumstellar material into a bipolar structure (Bollen et al. 2017).

The archetype of a classic SgXB is Vela X-1 where a NS is on an approximate nine-day eclipsing orbit around HD 77581, a B0.5 Ib Sg (Hiltner et al. 1972; Forman et al. 1973). The NS is deeply embedded in the intense stellar wind (with a mass loss rate $\dot{M}_\star \sim 6.3 \times 10^{-7} M_\odot \text{ yr}^{-1}$; Gimenez-Garcia et al. 2016) with an orbital separation of approximately 1.8 stellar radii (Quaintrell et al. 2003). The most recent observations revealed a terminal wind speed lower than initially claimed, on the order of 600–700 km s⁻¹, which is consistent with numerical computation from first principles (Sander et al. 2017a). These results suggest that orbital effects might dominate the dynamics between the stellar surface and the NS, and supply the wind with a significant amount of net angular momentum. It could lead to a complex accretion geometry that has a wind so beamed toward the accretor that it could share some features with the Roche lobe overflow mass transfer (RLOF) at stake in low mass X-ray binaries (LMXB). On the other hand, we know that in Cygnus X-1, a SgXB hosting a black hole, the O Sg donor star does not fill its Roche lobe (Orosz et al. 2011) and yet, even though the mass is transferred via the stellar wind, the accretor is surrounded by an accretion disk. These two systems suggest that the wind-RLOF regime (first studied in the context of symbiotic binaries by Mohamed & Podsiadlowski 2007) could be the appropriate framework to understand the structure of the accretion flow, rather than the BHL or RLOF geometries.

A consistent treatment of both the wind acceleration and its accretion by the compact object is thus needed to avoid being left with the wind speed in the vicinity of the accretor as a convenient but unconstraining degree of freedom. Sander et al. (2017a) computed the steady-state wind stratification for a 1D radial nonlocal thermal equilibrium atmosphere of a star representative of the donor star in Vela X-1. They accounted for a plethora of chemical elements and ionization levels susceptible to absorb the stellar UV photons and for the X-ray ionizing feedback from the accretor on the wind ionization state. In this paper, we intend to use this computed 1D line-driven acceleration to see how the 3D structure of the flow departs from a spherical wind once the orbital effects are added. Rather than being based on an empirical fitting formula, the wind velocity and density in the accretion region surrounding the accretor are mere consequences of the stellar and orbital properties. In Sect. 2, we evaluate the systematic bending of the wind streamlines by the orbital effects, as the wind develops and reaches the Roche lobe of the accretor with a nonzero net angular momentum. Within the Roche lobe, we run 3D hydrodynamical simulations described in Sect. 3 to capture the structure of the flow as it cools down downstream the shock and its capacity to form a disk-like structure. In Sect. 4, the

implications of such a component are discussed in the context of the SgXB Vela X-1 and Cygnus X-1.

2. Orbital deviation of the wind

2.1. Model and numerical method

Sophisticated models and simulations of the launching of line-driven winds show that they become supersonic shortly above the stellar photosphere and have Mach numbers typically above 5. This motivates a ballistic treatment of the wind bulk motion at the orbital scale: the trajectory of test-masses is integrated assuming the star and accretor are on circular orbits and that stellar rotation is synchronized with the orbital period. The 3D equation of motion in the corotating frame is

$$\mathbf{v} \frac{d\mathbf{v}}{dr} = \mathbf{a}_\star + \mathbf{a}_\bullet + \mathbf{a}_{\text{ni}}, \quad (1)$$

where \mathbf{a}_\bullet stands for the acceleration due to the NS gravitational field and \mathbf{a}_{ni} for the noninertial acceleration (centrifugal and Coriolis). The effective acceleration linked to the donor star of mass M_\star , once projected on the radial unity vector of the spherical frame of the star, is given by

$$a_\star = -GM_\star/r_\star^2 + a_{\text{rad}}(r_\star) + a_{\text{press}}(r_\star), \quad (2)$$

where r_\star is the distance to the stellar center and a_{press} is the acceleration due to thermal and turbulent pressure, which are important near the stellar photosphere. The term a_{press} is important to mitigate the bias introduced by the ballistic treatment in the immediate vicinity of the photosphere, where the wind is mildly supersonic. To describe a_{press} and the total radiative acceleration a_{rad} , with both the line and total continuum contribution, we rely on the computation by Sander et al. (2017a) for Vela X-1. Using the stellar atmosphere code PoWR (Hamann & Koesterke 1998; Gräfener et al. 2002), these authors calculated an atmosphere model for the donor star assuming a spherical, stationary wind situation. The radiative transfer is performed in the comoving frame, thereby the authors obtain the radiative acceleration without any further assumption or parametrization, i.e.,

$$a_{\text{rad}}(r_\star) = \frac{4\pi}{c} \frac{1}{\rho(r_\star)} \int_0^\infty \chi_\nu H_\nu d\nu, \quad (3)$$

where c is the speed of light and ρ is the mass density, deduced from the stellar mass loss rate and the velocity using the conservation of mass. The parameters χ_ν and H_ν denote the extinction coefficient (in cm⁻¹) and the Eddington flux at the frequency ν . Using the technique described in Sander et al. (2017b), the model provides a hydrodynamically consistent stratification, meaning that the mass loss rate and the velocity field were iteratively updated such that eventually the outward and inward forces balance each other throughout the stellar atmosphere. The wind velocity profile is expected to follow the β -law, which depends on the terminal speed v_∞ and on a β exponent that quantifies how quickly the terminal speed is reached as follows:

$$v_\beta(r) = v_\infty (1 - R_\star/r)^\beta. \quad (4)$$

However, the velocity and density stratification computed show notable deviations from this law, especially within a couple of stellar radii where the obtained wind velocity is lower than previously estimated (see the radial velocity profiles in Fig. 5 of Sander et al. 2017a). In SgXB, the orbiting accretor lies precisely in this region; hence there is a need to evaluate the impact

of the presence of the orbiting accretor on the structure of a slow wind. We note that in spite of the nonspherical situation due to the presence of the NS, we adopt a_{rad} as a_{press} as functions of the distance r_* to the donor star here for the sake of simplicity. It means that we neglect the feedback of the nonradial trajectories on the line acceleration magnitude and orientation. For highly nonradial winds, it is probably the main source of inaccuracy, but 3D radiative hydrodynamical simulations including the population numbers of the different energy levels of the ions from the statistical equilibrium equations are currently out of computational reach.

The streamlines computation is performed using the code developed in [El Mellah & Casse \(2016\)](#), starting from the stellar surface whose ellipsoidal deformation, even for Roche lobe filling factors close to unity, is not included since it is expected to have a negligible impact on the formation of a wind-captured disk. An illustration of the result is given in [Fig. 1](#) where the streamlines have been represented in the orbital plane. We stop the integration when the test-masses reach a sphere around the accretor $\sim 30\%$ larger than its Roche lobe radius. This strategy alleviates the difficulty of an a priori estimate of the accretion radius (the critical impact parameter below which test-masses are captured in the BHL formalism, [Edgar 2004](#)). It delimits the space where the ballistic approximation no longer holds. Dissipative effects at shocks are accounted for within this region in [Sect. 3](#). With this procedure, we focus on the fraction of the flow susceptible to be eventually accreted rather than on an accurate representation of the accretion tail in the wake of the accretor (for this component, see rather [Manousakis et al. 2014](#)).

The wind terminal speed is expected to scale approximately as the effective escape velocity; i.e., once surface gravity has been corrected for radiative continuum pressure on free electrons via the Eddington parameter. [Vink et al. \(2001\)](#) showed that for stellar effective temperatures above ~ 25 kK, the proportionality constant is twice higher than below, leading to a sharp drop of the terminal wind speed toward lower temperatures. The donor star in Vela X-1, HD 77581, is a B0.5 Ib Sg star ([Hiltner et al. 1972](#); [Forman et al. 1973](#)) whose effective temperature is ~ 25 kK. [Gimenez-Garcia et al. \(2016\)](#) suggested that it could explain the low terminal speed of $700 \text{ km s}^{-1} \pm 100 \text{ km s}^{-1}$ they measured for the wind of HD 77581. The computation carried out by [Sander et al. \(2017a\)](#) for HD 77581 also leads to terminal speeds ranging from 400 to 600 km s^{-1} depending on the inclusion of X-ray illumination from the accretor. A decisive result of their analysis is that the latter modifies the ionization state of the metal ions in the wind but does not necessarily inhibit the acceleration process. On the contrary, far enough upstream the NS, the effective absorption of UV photons might be locally enhanced once the metal ions are in a higher ionization level. Only close to the accretor, once all the elements have been deprived of their electrons, can the line-driven acceleration be halted, as previously emphasized in the literature (see, e.g., [Hatchett & McCray 1977](#); [Ho & Arons 1987](#); [Blondin et al. 1990](#); [Karino 2014](#); [Krticka et al. 2018](#)). In an attempt to illustrate the dramatic impact of the efficiency of the line-driven acceleration on the subsequent properties of the accretion flow, and to encompass potential inaccuracies in the calculation of this acceleration in the context of Vela X-1, we consider the case of an artificially enhanced wind acceleration (by 50%), which leads to larger flow velocities by approximately 20%. It could be caused, for instance, by a different chemical composition of the stellar atmosphere than that assumed in [Sander et al. \(2017a\)](#). In [Sect. 3](#), we see that the orbital speed is a threshold that separates two types of accretion flows and given the value of the orbital

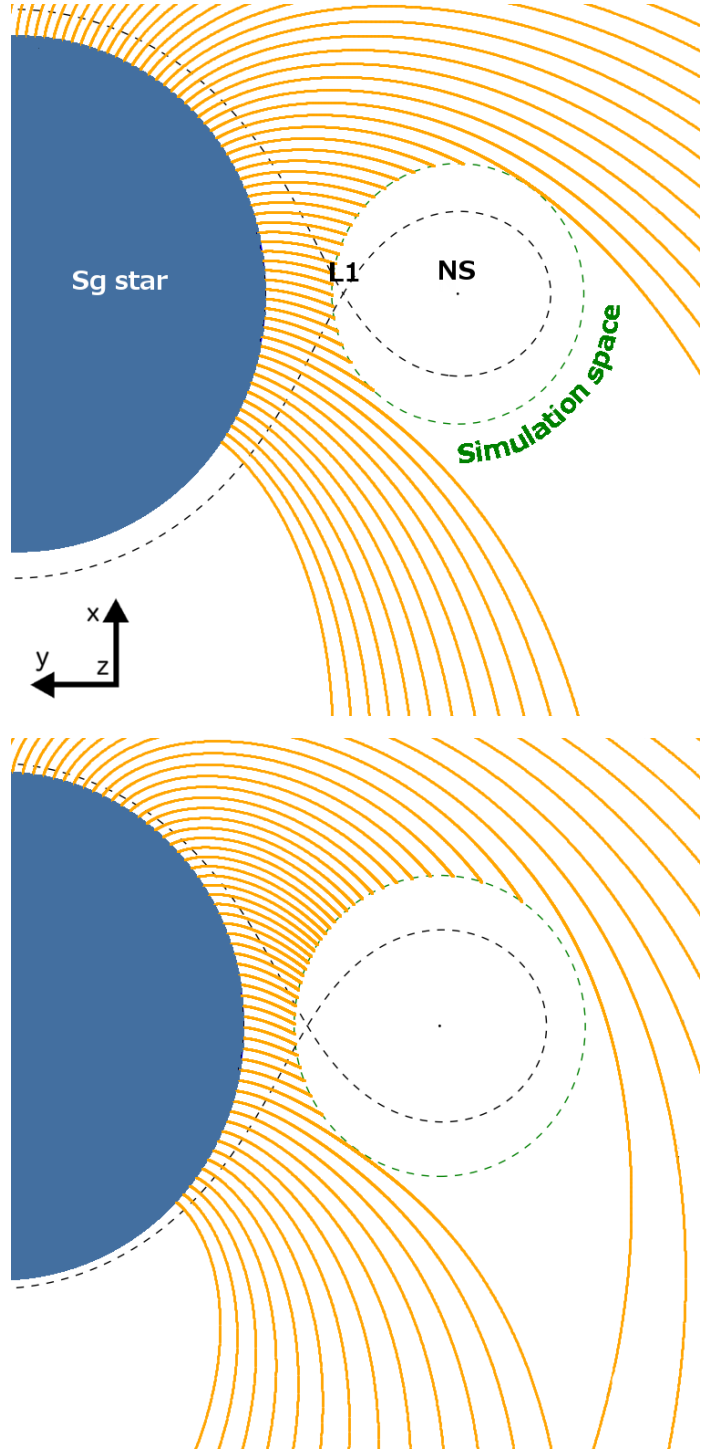


Fig. 1. In the orbital plane of the co-rotating frame, a few computed streamlines (orange) from the blue Sg to the HD simulation space (green dashed circle), centered on the accreting NS. The black dashed lines represent the critical Roche surface passing by the first Lagrangian point (L_1). *Upper panel* (resp. *lower*) is for the light fast (resp. heavy slow) configuration.

speed in Vela X-1 ($\sim 284 \text{ km s}^{-1}$); this enhancement of the wind acceleration induces major changes. From now on, we consider the following two cases in [Table 1](#):

- Heavy slow (HS): the accretor is heavy, with a mass of $M_* = 2.5 M_\odot$, lying on the upper edge of the expected maximum mass for a NS, and the radiative acceleration efficiency is not enhanced, leading to a relatively slow wind.

- Light fast (LF): the accretor has a mass of $M_{\bullet} = 1.5 M_{\odot}$ and the radiative acceleration efficiency is enhanced by 50%.

Since the NS mass estimates in Vela X-1 range from $1.7 M_{\odot}$ (Rawls et al. 2011) up to $2.3 M_{\odot}$ (Quaintrell et al. 2003), partly due to the uncertainty on the inclination of the system, we expect the real configuration to lie in between the two cases we consider.

2.2. Inhomogeneity and asymmetry of the wind

We now monitor the asymmetry and inhomogeneity of the flow when it reaches the spherical HD simulation space centered on the compact object and corresponding approximately to its Roche lobe. The aforementioned ballistic integration supplied information on the velocity vector at the surface of this sphere while the density relative to that at the stellar photosphere is deduced from the divergence of each streamline. This information is then binned on angular tiles; the polar axis of the spherical frame is aligned with the orbital angular momentum axis (\hat{z} in Figs. 1 and 2). In Fig. 2, we represented Mollweide projections of the local mass and angular momentum inflow at the surface of this space for the HS and LF cases: it offers an overview of the properties of the flow entering the accretor Roche lobe, seen from the accretor.

Concerning the integrated values at the inflowing edge of the simulation space, we focus on the mass inflow rate \dot{M}_{out} , the net specific (i.e., per unit mass) angular momentum of the flow l_{out} , and its corresponding circularization radius R_{circ} . The circularization radius is the radius at which a circular Keplerian orbit around the accretor would have the same specific angular momentum, i.e., $R_{\text{circ}} = l_{\text{out}}^2 / GM_{\bullet}$. The values are given in Table 1 and compared respectively to the stellar mass loss rate \dot{M}_{\star} , to the orbital specific angular momentum $a^2\Omega$, and to the NS magnetosphere radius R_{mag} (see, e.g., Frank et al. 1986),

$$R_{\text{mag}} \sim 1.4 \times 10^9 \text{ cm} \left(\frac{\rho}{10^{-12} \text{ g cm}^{-3}} \right)^{-1/6} \left(\frac{v}{2000 \text{ km s}^{-1}} \right)^{-1/3} \dots \left(\frac{B_{\bullet}}{2.6 \times 10^{12} \text{ G}} \right)^{1/3} \left(\frac{R_{\bullet}}{10 \text{ km}} \right), \quad (5)$$

where the values used for the mass density ρ and the flow speed v are orders of magnitude at the outer edge of the magnetosphere. The low dependence of the magnetosphere radius on these parameters guarantees that their exact values do not significantly alter this estimate. A typical NS radius has been used and the NS magnetic field is that deduced by Fürst et al. (2014) in Vela X-1. In Table 1, we used $R_{\text{mag}} = 1.4 \times 10^9 \text{ cm}$. We expect any disk-like structure to be truncated approximately at the inner radius (Ghosh & Lamb 1978) while quasi-spherical accretion onto the magnetosphere would proceed as described by Shakura et al. (2013). We note that the mass inflow rates shown in Table 1 set upper limits only on the final rate at which matter is accreted since only a subset of the streamlines entering the Roche lobe of the accretor is eventually accreted. However, it is already striking to notice how much more important the fraction of the stellar wind entering the simulation space in the HS configuration is compared to the LF one. The difference is essentially due to a significantly more important contribution of the high latitude region in the former case. Concerning the angular momentum, it might still vary within the simulation space since the forces are not isotropic around the accretor. The results shown in Table 1 show this. Within the current uncertainties on the mass of the accretor and efficiency of the wind launching process in Vela X-1, the two cases lead to dramatically different accretion flow configurations, in spite of their apparently similar parameters. In the HS case, where the flow is slightly slower than

Table 1. Parameters representative of Vela X-1 (with the star indexed with \star and the NS with \bullet), described in the text.

	LF	HS
M_{\star}	20.2 M_{\odot}	
R_{\star}	28.4 R_{\odot}	
$P = 2\pi/\Omega$	8.964357 days	
a/R_{\star}	~ 1.8	
\dot{M}_{\star}	$6.3 \times 10^{-7} M_{\odot} \text{ yr}^{-1}$	
M_{\bullet}	1.5 M_{\odot}	2.5 M_{\odot}
Enhanced	Yes	No
$\dot{M}_{\text{out}}/\dot{M}_{\star}$	4%	17%
$l_{\text{out}}/a^2\Omega$	-1%	3%
$R_{\text{circ}}/R_{\text{mag}}$	4	30

Notes. The bottom part of the table lists integrated quantities at the outer edge of the simulation space for the 2 models considered (LF and HS).

the orbital speed, the mass inflow rate within the Roche lobe of the accretor is four times larger, while the circularization radius is almost an order of magnitude larger than in the LF case, where the flow is slightly faster than the orbital speed.

In the left panels in Fig. 2, we see that the bulk of the mass inflow is approximately distributed in the same way in both cases and has a larger off-plane contribution when the wind is slower. This is the first hint that the inertia of the wind is no longer large enough to overcome the orbital flattening induced by rotation, a feature that has major consequences within the shocked region. In both cases, the incoming flow is centered around a mean radial direction which departs from the axis joining the compact object to the star (central cross in Fig. 2). The main difference though lies in the distribution of angular momentum inflow (right panels): the LF case leads to an equivalent amount of positive and negative angular momentum, which shows the essentially planar (albeit deviated) structure of the flow, whereas the HS case displays a large unbalance. The evaluation of the net angular momentum inflowing was in no case obvious a priori. The flow arriving from the first Lagrangian point L_1 (with positive angular momentum) is denser than the flow arriving from the right of L_1 as seen from the accretor (with negative angular momentum), but it is also slower. The present analysis shows that the former effect eventually dominates. The nonzero net angular momentum in the HS case cannot be attributed to an asymmetry of the mass inflow. Rather, it is due to the shift between the mean direction of arrival of matter (yellow spot in mass inflow maps) and the direction of radial inflow (white stripe in between blue and red in angular momentum inflow maps). It is much more significant for HS than for LF. Consequently, the net amount of specific angular momentum is larger for HS, which also leads to larger circularization radii and to the likelier presence of a wind-captured disk. We not put this prediction to the test.

3. Wind-captured disks

3.1. Physics and numerical setup

3.1.1. Equations

Within the Roche lobe of the accretor, we solve the nonviscous HD equations in their conservative form, converting accordingly the gravitational, radiative, and noninertial accelerations in the ballistic equation of motion (1) into forces per unit volume. In a first model, we solve the adiabatic energy equation everywhere, assuming that the heating from the donor star and X-rays

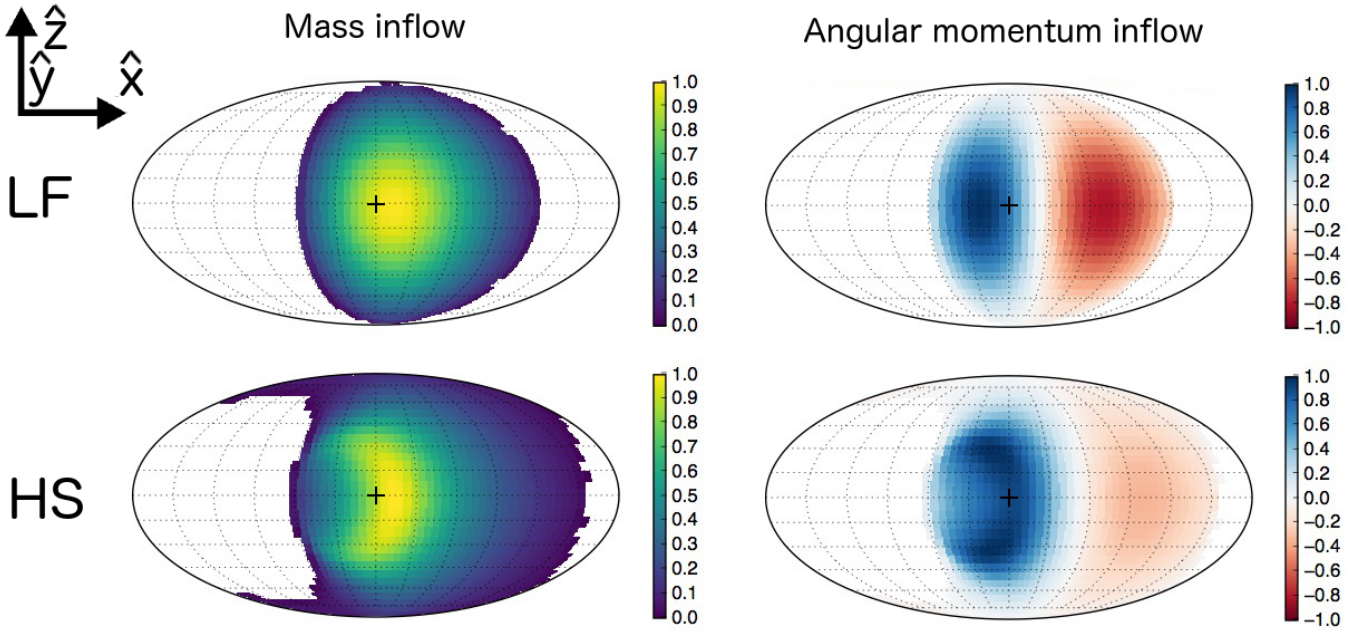


Fig. 2. Mollweide projections of local mass and angular momentum inflows within the simulation space centered on the accretor (dashed green sphere on Fig. 1). The *upper row* corresponds to the light fast (LF) case while the *bottom row* is for the heavy slow (HS) case. Each map is scaled to its maximum (absolute) value and centered on the axis from the accretor to the donor star (central dark cross). No mass inflow is measured in the white angular regions of the left maps (i.e., they are not reached by any of the ballistic streamlines). Positive (resp. negative) values of angular momentum stands for locally prograde (resp. retrograde) flow with respect to the orbital motion.

produced in the vicinity of the accretor balance the cooling of this optically thin supersonic wind. In Sect. 3.1.2, we discuss the validity of this adiabatic approximation downstream the forming shock and a way to relax this assumption. As is customary, we close the system of equations by assuming an ideal gas with an adiabatic index $\gamma = 5/3$.

The computation is performed with the finite volume code MPI-AMRVAC (Xia et al. 2018), using a third order HLL solver (Toro et al. 1994) with a Koren slope limiter (Vreugdenhil & Koren 1993). The spherical mesh we set up is an extension of what has been developed for an axisymmetric 2D flow in El Mellah & Casse (2015). The mesh is centered on the accretor and radially stretched to guarantee a constant relative resolution from the outer to the inner edge of the simulation space, spanning several orders of magnitude at an affordable computational cost and with a uniform cell aspect ratio. The outer radius of the simulation space is approximately half of the orbital separation, which is ~ 0.2 AU in Vela X-1, while the inner edge has a radius of five times the NS magnetosphere radius given by Eq. (5), hence a factor of approximately 200 between the inner and outer edge. Because of the symmetry of the problem above and below the orbital plane, we consider only the upper hemisphere and work with a resolution of $128 \times 32 \times 128$ corresponding to cells of aspect ratio close to unity near the equatorial plane of the mesh. Since our aim is to identify the conditions suitable for the formation of a wind-captured disk, the conservation of angular momentum is of uttermost importance. We implemented an angular momentum preserving scheme that guarantees the conservation of the component of the angular momentum projected onto the polar axis, in particular in the innermost regions of the flow, to machine precision. Instead of solving for the azimuthal component of the linear momentum, we consider the projection of the equation of conservation of angular momentum along the polar axis of the spherical frame (similar to what was done in polar coordinates by Molteni et al. 1999), i.e.,

$$\begin{aligned} \partial_t L_z + \frac{1}{r^2} \partial_r (L_z v_r r^2) + \frac{1}{r \sin^2 \theta} \partial_\theta (L_z v_\theta \sin^2 \theta) \\ + \frac{1}{r \sin \theta} \partial_\phi (L_z v_\phi) + \partial_\phi P = \Sigma, \end{aligned} \quad (6)$$

where t stands for the time coordinate, r , θ , and ϕ are the classic spherical coordinates in the frame centered on the accretor, ρ is the mass density, P the thermal pressure, and v_r , v_θ , and v_ϕ are the radial, polar and azimuthal components of the velocity, respectively. The value Σ is the source term due to the nonisotropy of the potential around the NS, which we do not describe explicitly in this work. Finally, $L_z = \rho r v_\phi \sin \theta$ is the angular momentum per unit volume projected on the polar axis. Since no geometrical source term is left after spatial (and time) discretization, numerical conservation of the polar component L_z of the angular momentum is guaranteed.

3.1.2. Radiative cooling

We estimate the importance of cooling in this physical environment. Upstream the shock, we rely on the temperature stratification derived from the solution of the statistical equilibrium equations and the radiative transfer. Based on the assumption of radiative equilibrium, the (electron) temperature structure in the expanding atmosphere is obtained by applying a generalized Unsöld-Lucy method described in Hamann & Koesterke (1998). Including the X-ray irradiation on the donor star leads only to a moderate increase of the temperature profile upstream the accretor compared to what was obtained in Sander et al. (2017a). Downstream the shock, we assume that the gas is optically thin and write the timescale τ_c to radiate away the internal energy,

$$\tau_c = \frac{nk_B T}{n^2 \Lambda(T)}, \quad (7)$$

where k_B is the Boltzmann constant, T is the temperature, n the Hydrogen number density, and $\Lambda(T)$ the cooling rate computed

by Schure et al. (2009), which includes the proportion of electrons relative to protons. If τ_d is the dynamical timescale for free fall at a fiducial accretion radius R_{acc} of $1/30^{\text{th}}$ of the orbital separation in Vela X-1, we obtain

$$\frac{\tau_c}{\tau_d} \sim 0.01 \left(\frac{T}{10^6 \text{ K}} \right) \left(\frac{\Lambda}{10^{-22} \text{ erg s}^{-1} \text{ cm}^3} \right)^{-1} \dots \left(\frac{\rho}{10^{-13} \text{ g cm}^{-3}} \right)^{-1} \left(\frac{M_\bullet}{2 M_\odot} \right)^{1/2} \left(\frac{R_{\text{acc}}}{0.2 \text{ AU}/30} \right)^{-3/2}, \quad (8)$$

where we use the values of temperature and density measured downstream the shock in the adiabatic simulations presented in Sect. 3.2.1. Unless the wind is a few times faster than expected in Vela X-1 and/or the star displays a mass loss rate an order of magnitude lower than what models and observations indicate, the flow is dense enough to cool significantly in the shocked region.

In an optically thin environment, we could in principle include radiative cooling using the module developed for MPI-AMRVAC by van Marle & Keppens (2011). Given the aforementioned ratio, it would lead to a cooling of the flow down to a floor temperature set by the X-ray and stellar radiation heating. Also, the optically thin approximation might not hold within the shocked region, especially when runaway cooling occurs and a high density disk-like region forms. As such, we chose to represent the cooling in a simpler way, using a polytropic model. It is equivalent to assume that the ratio of energy radiated away by the work done by the pressure force is constant: a certain compression leads to a certain energy loss, ranging from 0 (in the adiabatic limit) to 100% (in the isothermal limit) of the work done by the pressure force (Christians 2012). Above a certain threshold temperature T_0 , reached only within the shocked region, we overwrite the solution for the internal energy computed by the energy equation with the corresponding value of pressure deduced from the polytropic relation

$$P = C\rho^\alpha. \quad (9)$$

Provided there is no creation of entropy (in particular no shock), C is constant and uniform. In this framework, the polytropic index α ranges from 1 in the isothermal limit to γ in the adiabatic limit (Horedt 2000). After exploring a range of possible values for C and α , we retained three different cooling models as follows:

- Isentropic (or “isoS”): Cooling occurs only in a thin unresolved radiative layer immediately downstream the shock and is then negligible (for instance, because of intense X-ray heating), which means $\alpha = \gamma$ and a constant C set to a few percent of the entropy the flow would acquire downstream the shock in the fully adiabatic case, S_0 . The value T_0 is set to 10^6 K.
- Isothermal hot (or “hot”): Above $T_0 = C = 10^6$ K, the net cooling is efficient enough to compensate any adiabatic compression as the flow accretes, which leads to an isothermal flow ($\alpha = 1$).
- Isothermal cool (or “cool”): Same as previous but with a temperature $T_0 = 10^5$ K.

In the two isothermal cases, the cooling prescription means that the flow evolution is fully adiabatic until it reaches the temperature $T_0 = C$ when it becomes isothermal. We believe that including optically thin cooling without heating would lead to results qualitatively similar to the isothermal prescription we introduce in this work (as noticed by Saladino et al. 2018). The four models (fully adiabatic, isentropic, isothermal hot and cool) are summarized in Table 2.

Table 2. Parameters of cooling prescriptions in the four models.

	Adiabatic	isoS	Hot	Cool
Cooling	No	Yes	Yes	Yes
T_0	–	10^6 K	10^6 K	10^5 K
C	–	S_0	T_0	T_0
α	–	γ	1	1

3.2. Flow morphology

3.2.1. Adiabatic evolution

In Fig. 3, we represent slices in the orbital plane of the numerically relaxed state reached by the simulations. A 3D representation is shown in Fig. 4 to illustrate the level of beaming of the flow in the orbital plane.

In the case of a light accretor capturing material from a fast wind (LF configuration, upper panel in Fig. 3), the main features depart little from what has been observed in simulations of axisymmetric uniform flows. In agreement with Blondin & Raymer (2012), we do not observe any transverse oscillation of the tail (the so-called “flip-flop instability” that arises mostly in 2D polar numerical setups; Foglizzo et al. 2005). The orbital effects deflect the wind whose mean direction of arrival is $\sim 20^\circ$ misaligned with respect to the axis joining the star to the compact object. However, as discussed in Sect. 2.2, the flow remains essentially planar around this direction. When the flow is sufficiently beamed toward the accretor, it forms a bow shock (semitransparent blue surface in Fig. 4) at a distance ahead of the accretor that is compatible with a fraction of the accretion radius (Edgar 2004). The Mach-1 surface and the cone of density jump are slightly misaligned with each other; the side facing the star is denser. The Mach number immediately upstream the shock reaches 30 and we retrieve the classic jump conditions for an adiabatic shock. Between the outer boundary upstream and the inner boundary, the density (resp. the temperature) increases by a factor of ~ 100 (resp. 5000). In the innermost regions of the flow, we retrieve the sonic surface although it is no longer anchored into the inner boundary, contrary to what was predicted for a planar uniform flow with $\gamma = 5/3$ by Foglizzo & Ruffert (1996).

In the case of a heavy accretor capturing material from a slow wind (HS configuration, lower panel in Fig. 3), the morphology of the flow is dramatically different. Not only is the mean direction of arrival of the flow more misaligned with the line joining the star to the compact object ($\sim 45^\circ$), but also the shearing is much more important, leading to a significant amount of net angular momentum. A bow shock also forms but while it extends over several accretion radii on the side where the flow is less dense and faster, the beamed wind arriving directly from L_1 remains mildly supersonic as it passes the accretor. It is strongly deflected and accelerated by the gravitational slingshot but only to finally impact the shocked region from the back. The adiabatic compression it first experiences leads to a dense and fairly cool region compared to the innermost parts of the flow. We also notice that when the wind is slower, material from higher latitudes on the star contributes to the accretion process, as shown by the vertical extent of the mass inflow map in Fig. 2; the beaming of the wind in the orbital plane builds up the red dark bulge observed on the right in Fig. 4. It is a specific feature of wind-RLOF configurations since in pure RLOF only matter from the vicinity of L_1 flows in the Roche lobe of the accretor, while in pure wind configurations the centrifugal force is too weak to

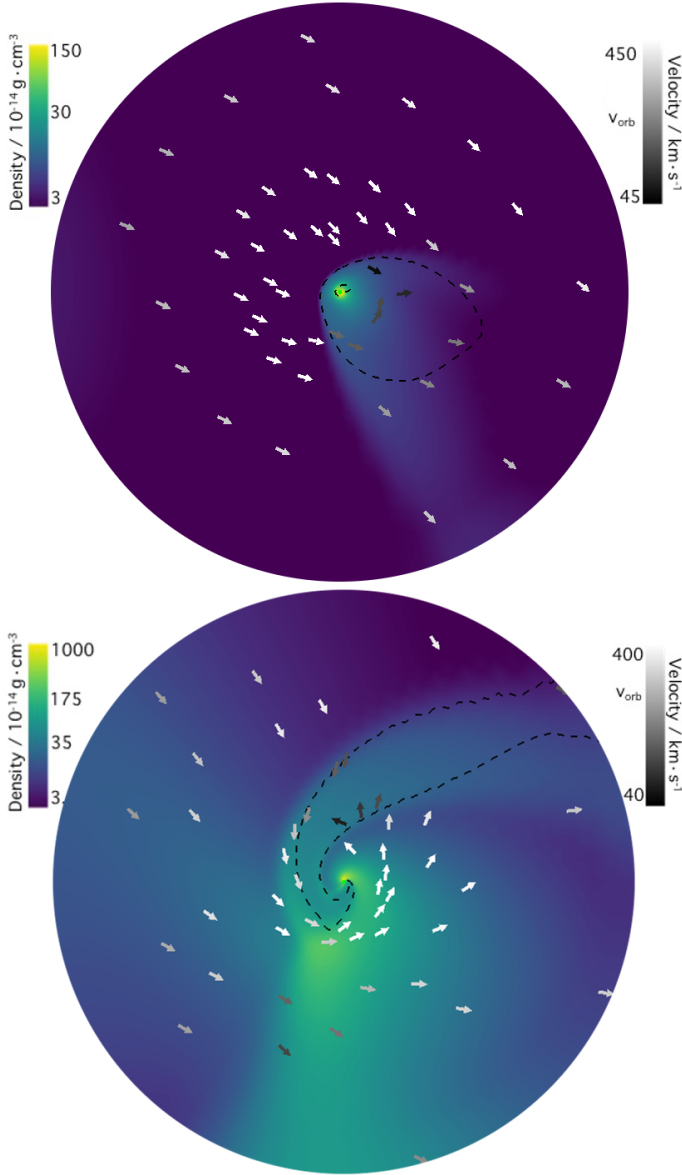


Fig. 3. Logarithmic color maps of the density field in the orbital plane. The arrows stand for the velocity field; the black to white color map indicates their increasing magnitude. The orbital speed of Vela X-1, $v_{\text{orb}} \sim 284 \text{ km s}^{-1}$, is represented (linear scale). The black dashed line indicates the Mach-1 contour. The radial extension of the simulation domain relative to the orbital separation corresponds to the green dashed delimited regions in Fig. 1, which is approximately the Roche lobe of the accretor. *Bottom panel:* LF configuration. *Top panel:* HS configuration.

focus the fast wind in the orbital plane and the wind at high stellar latitudes does not participate in the accretion process. Downstream this bulge, as seen in Fig. 4, the shocked region of the HS setup presents a characteristic spiral shape that delimits a narrow accretion channel along which matter flows in (resp. out) beyond (resp. below) the stagnation point. The orientation of this stream differs in its orientation with that observed in RLOF systems due to the much lower effective gravity of the donor star (after including the line radiation and pressure accelerations), which alters the classic Roche potential we rely on in LMXB.

Although the Mach number of the flow entering the simulation space remains below 10 owing to the limited efficiency of the wind acceleration, just upstream the shock Mach numbers of 20 are reached; this leads to a temperature jump of approxi-



Fig. 4. Three-dimensional contours of the mass density for the LF (semitransparent blue) and HS (red) configurations. The black arrow indicates the approximate direction of the arriving wind, while the vertical direction is aligned with the orbital angular momentum. We note the axisymmetry of the LF flow structure around the mean direction of wind arrival, whereas the HS flow is compressed in the orbital plane and forms a characteristic channel reminiscent of the stream of matter in RLOF systems. Same scale as Fig. 3.

mately 400. As the flow is accreted, the corresponding temperatures on the order of 10 MK keeps increasing up to 100 MK at the inner boundary. This temperature, close to the relativistic regime, is unphysical in this context and a mere consequence of the adopted adiabatic treatment; however, as already discussed in Sect. 3.1.2, a more realistic one would also include effects of radiative cooling in the simulations.

3.2.2. Polytropic cooling

We now study the influence of cooling on the morphology of the flow in the LF and HS cases. Whatever cooling prescription invoked, the LF setup never leads to the formation of a disk-like structure around the accretor. Instead, triggering the cooling for the LF flow leads to a serious recession of the front shock, down to the inner boundary of the simulation space, due to a drop of the pressure built-up downstream the shock. With the isentropic prescription, we ran a simulation with an inner boundary 5 times smaller to make sure that the size of the inner boundary was not impacting the morphology of the flow, and the result remained unchanged. Since the magnetic field is believed to play a role so close from the accretor and our simulations are only HD, we are not able to make any statement on the following accretion of the flow in the LF case, except that it is bound to not proceed via a disk. From now on, “LF” refers to the LF configuration coupled with the isentropic cooling prescription.

On the contrary, in the HS configuration the front shock holds and a permanent disk-like structure forms within the shocked region for all cooling prescriptions used (see Fig. 5). In the isentropic case, the hull of the shock remains essentially unchanged, including the density bulge, since the cooling is only triggered in the innermost region, where the temperature of the flow goes beyond $T_0 \sim 1 \text{ MK}$. There, we observe the formation of a flattened persistent structure, partly supported by the centrifugal force (see Fig. 6). In a disk, the thickness aspect ratio

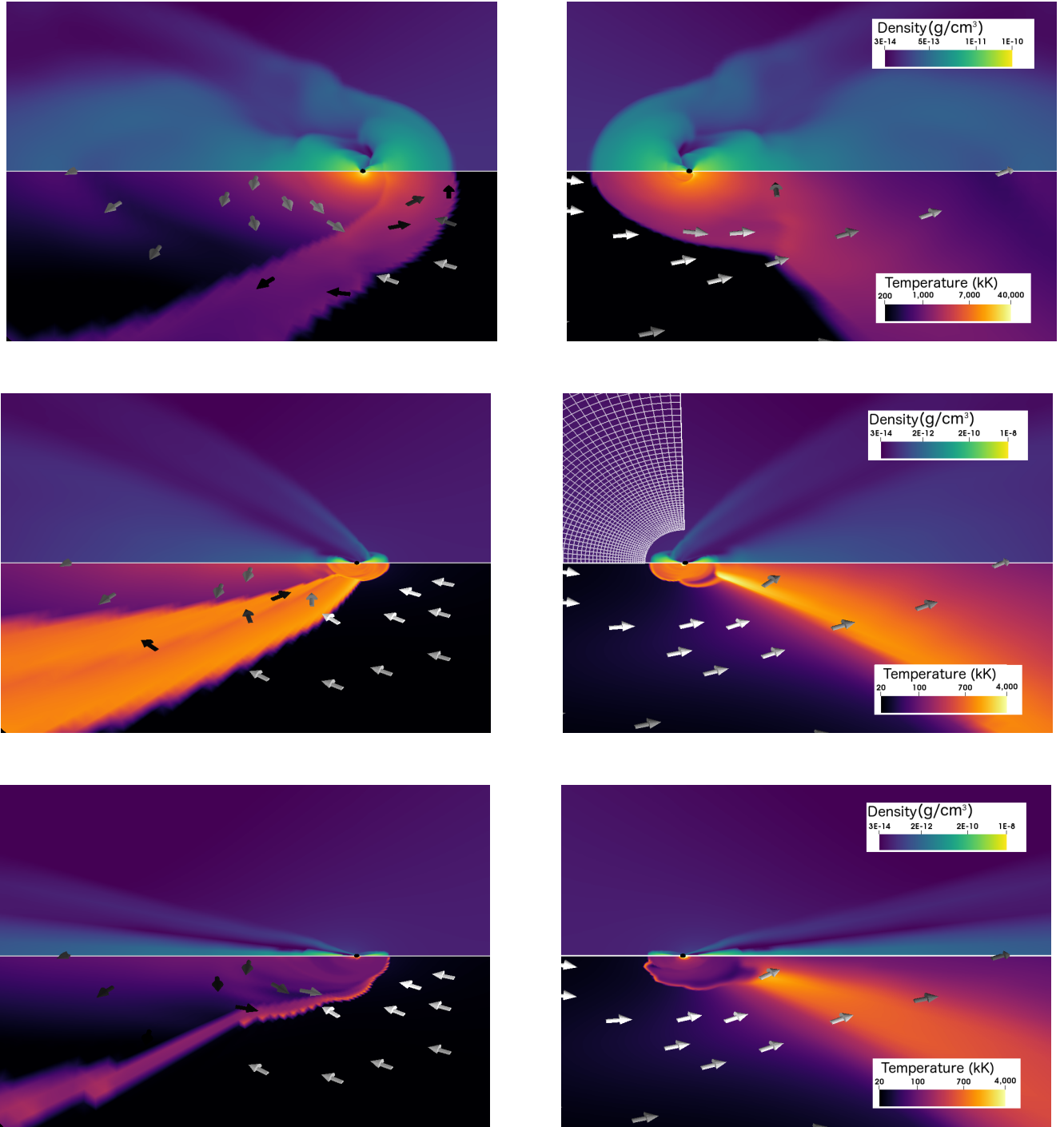


Fig. 5. Side views of the flow structure when cooling is triggered using an isentropic (*upper panels*) or an isothermal prescription, with a high temperature (*middle panels*) or low temperature (*lower panels*). In the *left* (resp. *right*) column, the wind comes from the right (resp. *left*). The lower half of each panel shows a logarithmic thermal color map in the orbital plane while the upper half represents the transverse (or “vertical”) logarithmic density distribution. We also plotted the velocity field in the orbital plane with a white to black color scale to indicate a slowing down by a factor of at least 4. The radially stretched mesh is represented to indicate the resolution.

(i.e., the ratio of the scale height by the distance to the central mass projected onto the disk midplane) is expected to scale as the ratio of the sound speed by the speed of a test-mass on a circular orbit (hereafter, the Keplerian speed). As indicated by the relatively large thickness aspect ratio of the disk ($\sim 50\%$), the pressure still plays an important role in sustaining the structure. Similarly, this disk-like structure appears in the two isothermal cases with a thinner disk for a lower temperature. From now on,

“cool”, “hot”, and “isoS” refer to the HS configuration coupled with the corresponding cooling prescription.

Another way to appreciate whether the flow is centrifugally supported, and up to which radius, is to plot the longitudinal velocity profile in the orbital plane and to compare this velocity to the Keplerian velocity profile expected for a thin disk. In Fig. 7, it is clear that the LF case displays a flow speed (solid blue line) that is an order of magnitude below the Keplerian expectation (dashed

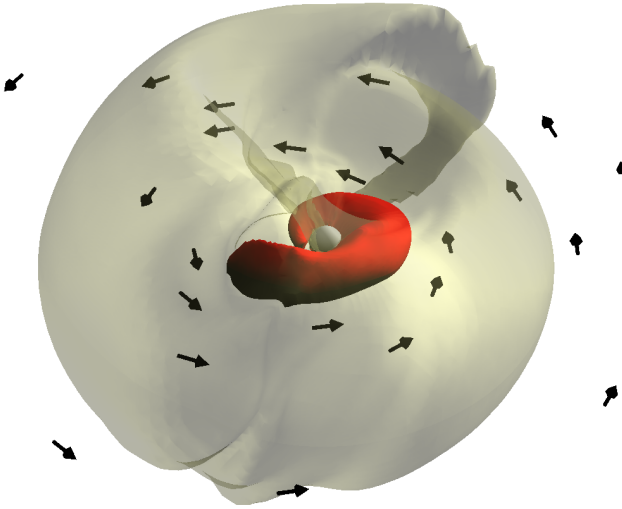


Fig. 6. Three-dimensional contours of the mass density for the isentropic HS configuration (upper panels in Fig. 5); the yellow semitransparent surface is 5 times less dense than the inner red surface. The arrows stand for the velocity field in the orbital plane. The flow comes from the upper left. Spiral arms are visible for each surface. The central white sphere stands for the inner boundary of the simulation space, ~ 200 times smaller than the outer boundary shown in Fig. 1.

blue), while the three HS cases show a much better match between the measured (red, green, and orange solid lines) and the Keplerian (black dashed) velocity profiles. Within the disk, the velocity profile is a power law because the profiles are straight lines; but once we reach the outer extent of the disk, a sudden change in slope occurs. A warmer disk corresponds to a larger extent of the disk. The hot and the cool cases yield disks with thickness aspect ratios of ~ 20 and 5%, respectively, and velocity profiles that decrease as $1/\sqrt{r}$, in agreement with a constant temperature and a power-law density profile. However, they display rotational speed approximately 15% above the Keplerian speed within the disk, which might be due to numerical effects at the inner border or representative of a not fully steady numerical state (see Sect. 4.1). In the isentropic case, we find a velocity profile decreasing faster than $1/\sqrt{r}$, which indicates an increasing importance of the thermal pressure in the equilibrium of this thicker disk, which agrees with the aforementioned large thickness aspect ratio.

Without cooling, we have seen that no disk formation is possible independent of the net angular momentum carried by the accreted flow. In the context of disk formation during common envelope phase, MacLeod & Ramirez-Ruiz (2015), MacLeod et al. (2017), and Murguía-Berthier et al. (2017) performed similar simulations of asymmetric BHL accretion using a single polytropic relation everywhere in the domain. These works concluded that disk formation was possible provided the flow was compressible enough, the compressibility being provided either by effective cooling or the capacity to convert a fraction of the energy released by compression to further ionize the stellar outer layers. Our results also agree with similar simulations of mass transfer in the context of binaries where the donor star is on the asymptotic giant branch (Huarte-Espinosa et al. 2012; Saladino et al. 2018). More generally, without energy loss, a flow with a given angular momentum cannot circularize. By analogy with a test-mass, it would keep orbiting on the highly eccentric orbit the initial conditions imprinted. The shock mediates this analogy by adding entropy to the flow, but internal energy needs to be radiated away to lead to the formation of a centrifugally supported structure.

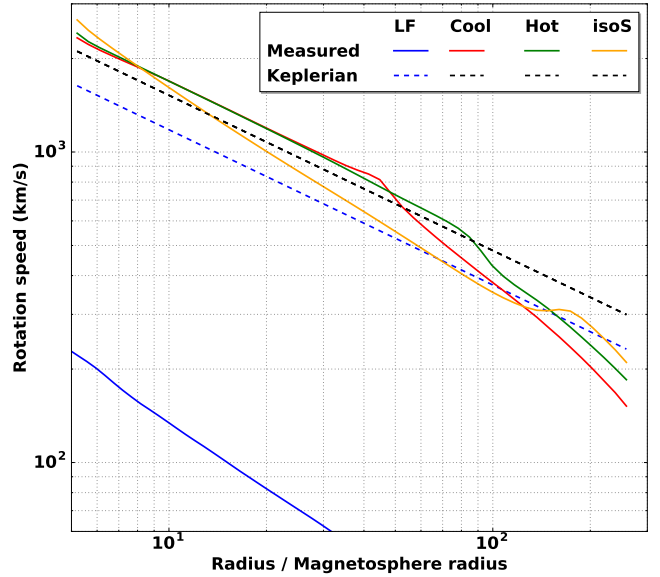


Fig. 7. Longitudinal velocity profiles in the orbital plane as a function of the distance to the accretor measured in units of the magnetosphere radius given in Eq. (5). The velocities of the LF (blue) and HS configurations (red, green and yellow) are measured once the numerically relaxed state is reached and averaged over the longitudinal angles. The measured velocity profiles (solid lines) are compared to the Keplerian profiles expected for a thin disk around the light and the heavy NS in dashed blue and dashed black, respectively.

4. Discussion and observational consequences

4.1. Accretion rates

4.1.1. Mass accretion rate

After at most a few crossing times, the total mass and angular momentum within the simulation space reach a plateau and the mass and angular momentum accretion rates do not vary by more than a few percent. The levels we observe depend significantly on the efficiency of the wind line-driven acceleration and on the mass of the accretor (LF and HS configurations). In Fig. 8, we represent the mass accretion rate at the inner boundary of the simulation space as a function of time. Comparing the HS and LF cases enables us to underline the dramatic increase in the mass accretion rate when the wind speed becomes similar to the orbital speed. While the mass accretion rate at the Roche lobe was approximately four times larger in the HS case (see Sect. 2.2), this rate is an order of magnitude higher in the HS case once it reaches the NS magnetosphere. The mass accretion rates shown in Fig. 8 are steady and, within the shocked region, fairly independent of the radius at which they are measured, in agreement with the conservation of mass.

Currently, accretion of matter within the inner border is enabled only by the evacuation of angular momentum through spiral shocks (visible in Fig. 6). However, in the absence of a proper treatment of the effective viscosity, statements on the absolute values of the mass accretion rate witnessed in these simulations should be taken with some caution. That said, the values we observe, on the order of a few $\dot{M} \sim 10^{-8} M_{\odot} \text{ yr}^{-1}$ would correspond to X-ray accretion luminosities on the order of $L_{\text{acc}} \sim \zeta \cdot 3 \times 10^{39} \text{ erg s}^{-1}$, where ζ encapsulates the information on the efficiency of the conversion process from kinetic energy to X-ray emission. Provided this coefficient reaches its maximum value given by the compactness parameter of the accretor (10–30% for a NS), the X-ray luminosity would be an order of

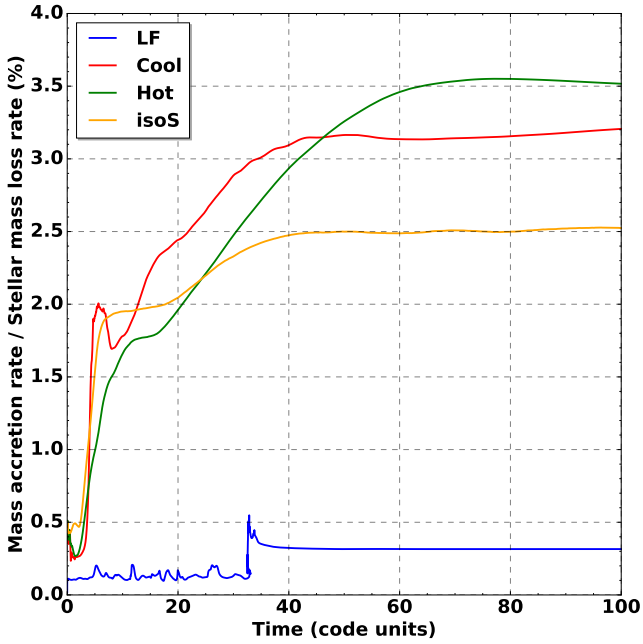


Fig. 8. Mass accretion rates at the inner border of the simulation space (at $\sim 5 R_{\text{mag}}$) as a function of time. In the case of the HS configuration, the mass accretion rate is significantly larger than in the LF case, whatever the cooling prescription.

magnitude higher than the Eddington luminosity L_{Edd} of a NS. In this case, accounting for the influence of the radiative force on the dynamics of the flow would be required to make reliable conclusions. Interestingly enough, it means that wind-RLOF, because it combines both the mass transfer efficiency of RLOF (usually associated with LMXB) and the large amount of available matter provided by the mass loss mechanism of a massive star (associated to HMXB), could lead to super-Eddington accretion. In particular, we notice that some ultra luminous X-ray sources (ULX) have been shown to be super-Eddington accreting NS (Bachetti et al. 2014; Fürst et al. 2016; Israel et al. 2017). Supergiant or Wolf-Rayet donor stars, such as those identified in some systems, could provide material at a rate sufficient to reproduce this X-ray luminosity (El Mellah et al. 2019).

Regarding the current systems of interest in this paper, classic SgXB and Vela X-1 in particular, it would be inconsistent with the observed X-ray luminosity ranging from 10^{35} erg s $^{-1}$ to a few 10^{37} erg s $^{-1}$ in Vela X-1 (Fürst et al. 2010). In the case of an accreting black hole, very low values of ζ can be reached for radiatively inefficient accretion flow, either because the flow has no time to cool or because it is optically thick enough to drag the radiation in its fall toward the event horizon (Narayan et al. 1998). But for a NS, the kinetic energy must be released before or at the impact with the NS surface (Medvedev & Narayan 2000). Very faint accreting NS have been identified in LMXB (Armas Padilla et al. 2013). In spite of a RLOF mass transfer that is susceptible to providing a large percentage of the Eddington mass accretion rate, these systems maintain low X-ray luminosities of 5×10^{34} to 5×10^{36} erg s $^{-1}$ (i.e., 10^{-4} to $10^{-2} L_{\text{Edd}}$) for years; these luminosities much below the levels generally observed in LMXB. Degenaar et al. (2017) reported on observational signatures of an outflow in one of these sources, IGR J17062–6143, and suggested two mechanisms to account for the low luminosity of the accreting NS. The first possibility could be a truncated disk with a radiatively inefficient accretion flow in the inner parts (see, e.g., the adiabatic inflow-outflow solution derived by Blandford & Begelman

1999), which is possibly associated with an outflow. An alternative scenario is a propeller-driven outflow. In the regions in which we monitored the flow, the magnetic field carried by the flow has little influence on the motion of the gas. However, when the flow gets close enough to the accretor, it gets highly ionized by the X-ray emission and encounters the intense dipolar magnetic field of the NS. From this point, the magnetic field takes over and controls the dynamics. In SgXB, any putative disk-like structure would eventually be truncated way before the NS surface (Ghosh & Lamb 1978). In the propeller regime, part of the matter falling onto the magnetosphere might eventually be repelled, leading to a much lower effective mass accretion rate than the amount inflowing at a few magnetosphere radii (Illarionov & Sunyaev 1975; Bozzo et al. 2008).

4.1.2. Angular momentum accretion rate

When a disk forms, the angular momentum accretion rate at a few R_{mag} can in no case be indicative of the torque applied to the accretor since accretion takes place thanks to the evacuation of a significant amount of angular momentum. However, it provides an upper limit that can be computed to monitor the consistency of these simulations. In addition, the characteristics of the exchange of angular momentum between the flow and the NS depends on the extent of the corotation radius with respect to the magnetosphere radius (Ghosh & Lamb 1979). A naive computation of the characteristic spin-up time τ_L of a NS of mass $M_{\bullet} = 2 M_{\odot}$, of radius $R_{\bullet} = 10$ km and of spin period $P_{\bullet} = 2\pi/\omega = 283$ s, which is representative of the NS hosted in Vela X-1, would give (with the angular momentum accretion rate \dot{L} we measure at the inner edge of the HS simulations),

$$\tau_L = \frac{L_{\bullet}}{\dot{L}} = \frac{M_{\bullet} R_{\bullet}^2 \omega^2}{\dot{L}} \sim 10 \text{ kyrs}, \quad (10)$$

which is one to three orders of magnitude smaller than the net spin-up or spin-down time observed reported in the literature (see, e.g., Ziolkowski 1985). This shows that the angular momentum flowing through the inner boundary of our simulation space is too large and that only the fraction that is not evacuated during the accretion process actually reaches the NS and play a role in spinning it up or down.

4.2. Disk extension and viscous lag: The case of Cygnus X-1

Even in systems that are known to harbor an accretion disk, we have often little insight on the disk outer radius. Indeed, most of the light comes from the innermost region; this emission, for a disk extending all the way down to the compact accretor, is emitted in X-rays in a waveband well separated from the stellar black-body emission. In RLOF systems, the monitoring of the hot spot can help to locate this outer ring, provided the disk is not tilted and theoretical limits exist on the maximum extension of the disk ($\sim 70\%$ of the Roche lobe radius of the accretor, Paczynski 1977).

Recently, Taam et al. (2018) invoked a hot, low angular momentum accretion flow to explain the absence of visible hysteresis in the hardness-intensity cycle of Cygnus X-1, where the contrast is low between the brightest and dimmest X-ray emission compared to BH in LMXB (Grinberg et al. 2014). Indeed, in Cygnus X-1, mass transfer most likely proceeds through wind accretion. Although focused on the case of a NS accretor, the present study indicates that if the wind speed is not negligible compared to the orbital speed, the disk should be smaller than

what a RLOF process would produce in a classic BH-LMXB. In Cygnus X-1, the donor star is of similar mass as in Vela X-1 but with a radius smaller by almost a factor of 2 (Orosz et al. 2011), which would lead, for a similar Eddington parameter, to a larger wind terminal speed if scaled as the effective escape speed at the stellar photosphere (as discussed in Sect. 2.1). But this increase must be compared to the orbital speed in Cygnus X-1 ($\sim 400 \text{ km s}^{-1}$), which is also larger than in Vela X-1, along with the much more important mass of the accretor relative to the donor star. All in all, the extent of the wind-captured disk formed in Cygnus X-1 might be larger than observed in the HS configuration, which is more suitable for Vela X-1, but much smaller than a RLOF formed disk. Smith et al. (2001) already pinpointed that the delay between the hard-to-soft and soft-to-hard transitions might be representative of the different propagation times in a two components accretion flow. While the corona reacts to a perturbation of a free-fall timescale, the disk, which is limited by the viscous timescale, would always lag behind. Because the viscous timescale depends on the outer extent of the disk, a lower delay in the hardness-intensity cycle of Cygnus X-1 compared to BH-LMXB would indicate a smaller disk extent; this is consistent with the present study of the properties of wind-captured disks. Similar time delay analysis also led Ghosh et al. (2018) to suggest a small disk extent in Cygnus X-1.

5. Conclusions

In this paper, we tried to evaluate the possibility of obtaining a wind-captured disk in SgXB and in particular in the classic NS - hosting SgXB Vela X-1. We connected the orbital scale at which the wind develops to that of the accretion radius, at which the flow is significantly beamed by the gravitational field of the compact object and where HD shocks form all the way down to the outer edge of the NS magnetosphere. With these simulations, we consistently cover the development of the wind as it is launched, compute its deviation at the orbital scale, and evaluate the fraction eventually reaching the NS magnetosphere. We showed that the wind dramatically departs from a radial outflow when the wind speed is as low as the orbital speed. We also captured the adiabatic bow shock that forms ahead of the accretor and characterized its highly asymmetric shape for a slow wind. Provided cooling is triggered in the shocked region and the accreted flow formed out of a slow wind circularizes at a few ten times the NS magnetosphere radius. The obtained disk-like structure is essentially maintained by the centrifugal force and displays a quasi-Keplerian rotation profile.

Currently, we face a lack of conclusive evidence of the presence of a permanent disk in SgXB hosting NS (Bozzo et al. 2008; Shakura et al. 2012; Romano et al. 2015; Hu et al. 2017). Yet, because of the truncation of the disk by the NS magnetosphere (Ghosh & Lamb 1978), we do not expect from it an emission as intense and as high energy as for a disk extending deeply into the gravitational potential of the compact accretor. In UV waveband, the emission from a putative disk would be dominated by the flux from the O/B Sg star, and in the X-rays accretion columns at the NS poles would be much brighter than the truncated disk. Alternatively, if the wind actually reaches speeds larger than the orbital speed upstream the accretor, a wind-captured disk would be ruled out by the present study. Taani et al. (2019) recently identified possible hints of accretion via a disk in 2 SgXB, OAO 1657-415, and LMC X-4. The latter has already been pinpointed in the literature as a possible disked SgXB. Based on their positions in the lower left end of the Corbet diagram (Corbet 1984) and on their high X-ray luminosities,

a disk is believed to have formed around the compact object in LMC X-4 as well as in Cen X-3 or SMC X-1 (Falanga et al. 2015). However, the large mass ratios (>10) in these systems suggest that a stable pure RLOF is unlikely, a inconsistency that could be solved by the present mass transfer mechanism; wind-RLOF remains stable for large mass ratios while still leading, for realistically slow winds, to the formation of a wind-captured disk around the accretor.

To summarize, in Vela X-1, we face two possible wind accretion scenarios:

- First, the line-driven wind acceleration is not efficient enough to provide the flow with a velocity larger than the orbital speed when it enters the Roche lobe of the accretor. In this case, the orbital effects control the dynamics of the wind which is seriously beamed and has a fraction of the stellar mass loss rate of larger than 10% entering the Roche lobe of the accretor. The flow quickly acquires angular momentum and within the shocked region, a disk-like structure is formed with thicker disks for less efficient cooling. Because Vela X-1 is an eclipsing system and since we expect the wind-captured disk to form within the orbital plane, the thickness of the disk might significantly alter the absorbing column density. In the case of an inefficient cooling, the disk would be thick enough to intercept the line of sight and contribute to the observed absorbing column density. Also, Foulkes et al. (2010) showed that the precession of a disk wrapped by a radiative pressure driven instability (Pettersen 1977a,b) could be responsible for the off-states observed in some systems, although mechanisms that do not rely on the presence of a disk have been proposed for Vela X-1 (see, e.g., Manousakis & Walter 2015).
- Second, the line-driven wind acceleration is more efficient than that computed for a 1D steady atmosphere in Sander et al. (2017a), for instance because of the significant influence of the departure from a purely radial wind or a different chemical composition of the donor star than assumed. For instance, among the most important driving elements of the donor star in Vela X-1, the abundances of N and Si are determined from spectral lines, but the abundances of S and Fe are just assumed to be solar (Gimenez-Garcia et al. 2016). Since the Fe forest is well reproduced, the abundances are thought to be accurate within a factor of at most 2. In the case of a more efficient wind acceleration, the LF configuration, which has a wind speed slightly larger than the orbital speed, would be more representative of the wind accretion process at stake in Vela X-1 and no disk structure would form. The mass accretion rate, on the order of a few 0.1% of the stellar mass loss rate, would be consistent with the observed mean X-ray luminosity for typical values of ζ (i.e., $\sim 5\text{--}10\%$).

Although we considered line-driven winds in this work, the condition on the ratio of the wind speed to the orbital speed to form wind-captured disks is also matched in some binary systems surrounded by a planetary or pre-planetary nebula. Consequently, RLOF is not required to form a disk around the accreting companion of an asymptotic giant branch star such as that studied in Bollen et al. (2017).

The present study addressed the permanent behavior of the flow, but winds of massive stars are unstable and form internal shocks that lead to overdense clumps of matter (Owocki & Rybicki 1984; Sundqvist et al. 2018). The impact of these clumps on the time variability of the mass accretion rate has been investigated in El Mellah et al. (2018), but these authors considered a wind fast enough to not be bent by the orbital

effects. The present work shows that, provided the wind speed is similar to the orbital speed, the orbital bending and the associated net angular momentum cannot be neglected. Because the clumps carry themselves a local angular momentum, [El Mellah et al. \(2018\)](#) showed that clumpy wind accretion was less efficient than its homogeneous counterpart; including the micro-structure of the wind might thus help to decrease the mass accretion rate at a few NS magnetosphere radii, but the influence of the clumps on the properties of the wind-captured disk (e.g., its permanence) remains to be studied. With a proper treatment of the effective viscosity in the disk and the coupling between the disk and the magnetosphere, we could produce a physically motivated synthetic curve of the torque applied to the NS as a function of time. This could open the door to a consistent way to address the question of the spin-up and spin down of the NS. Conversely, transfer of angular momentum via wind-RLOF could well play a decisive, long-term role in spinning up black holes as shown by [Moreno Méndez et al. \(2008\)](#) and [Moreno Méndez \(2011\)](#).

Acknowledgements. The authors thank the referee for her/his insights. IEM wishes to thank Antonios Manousakis for fruitful discussions about the underlying computational aspects and the members of the X-wind collaboration for the observational consequences of the present analysis. IEM also thanks Wenbin Liu for the insightful discussions on the accretion of angular momentum. IEM has received funding from the Research Foundation Flanders (FWO) and the European Union's Horizon 2020 research and innovation program under the Marie Skłodowska-Curie grant agreement No 665501. A.A.C.S. would like to thank STFC for funding under grant number ST/R000565/1. IEM and JOS are grateful for the hospitality of the International Space Science Institute (ISSI), Bern, Switzerland, which sponsored a team meeting initiating a tighter collaboration between massive stars wind and X-ray binaries communities. The simulations were conducted on the Tier-1 VSC (Flemish Supercomputer Center funded by Hercules foundation and Flemish government).

References

- Abbott, B. P., Abbott, R., Abbott, T. D., & Ai, E. 2016, *Phys. Rev. Lett.*, **116**, 241103
- Armas Padilla, M., Degenaar, N., & Wijnands, R. 2013, *MNRAS*, **434**, 1586
- Bachetti, M., Harrison, F. A., Walton, D. J., et al. 2014, *Nature*, **514**, 202
- Blandford, R. D., & Begelman, M. C. 1999, *MNRAS*, **303**, 1
- Blondin, J. M., & Raymer, E. 2012, *ApJ*, **752**, 30
- Blondin, J. M., Kallman, T. R., Fryxell, B. A., & Taam, R. E. 1990, *ApJ*, **356**, 591
- Bollen, D., Van Winckel, H., & Kamath, D. 2017, *A&A*, **607**, A60
- Bozzo, E., Falanga, M., & Stella, L. 2008, *ApJ*, **683**, 1031
- Castor, J. I., Abbott, D. C., & Klein, R. I. 1975, *ApJ*, **195**, 157
- Christians, J. 2012, *Int. J. Mech. Eng. Edu.*, **40**, 53
- Corbet, R. H. D. 1984, *A&A*, **141**, 91
- Decin, L., Ward, H., Danilovich, T., et al. 2019, *Nat. Astron.*, accepted
- Degenaar, N., Pinto, C., Miller, J. M., et al. 2017, *MNRAS*, **464**, 398
- De Marco, O. 2009, *PASP*, **121**, 316
- Duchêne, G., & Kraus, A. 2013, *ARA&A*, **51**, 269
- Edgar, R. G. 2004, *New Astron. Rev.*, **48**, 843
- El Mellah, I., & Casse, F. 2015, *MNRAS*, **454**, 2657
- El Mellah, I., & Casse, F. 2016, *MNRAS*, **467**, 2585
- El Mellah, I., Sundqvist, J. O., & Keppens, R. 2018, *MNRAS*, **475**, 3240
- El Mellah, I., Sundqvist, J. O., & Keppens, R. 2019, *A&A*, **622**, L3
- Falanga, M., Bozzo, E., Lutovinov, A., et al. 2015, *A&A*, **577**, A130
- Foglizzo, T., & Ruffert, M. 1996, *A&A*, **361**, 22
- Foglizzo, T., Galletti, P., & Ruffert, M. 2005, *A&A*, **2201**, 15
- Forman, W., Jones, C., Tananbaum, H., et al. 1973, *ApJ*, **182**, L103
- Foulkes, S. B., Haswell, C. A., & Murray, J. R. 2010, *MNRAS*, **401**, 1275
- Frank, J., King, A., & Raine, D. J. 1986, *Phys. Today*, **39**, 124
- Fürst, F., Kreykenbohm, I., Pottschmidt, K., et al. 2010, *A&A*, **519**, A37
- Fürst, F., Pottschmidt, K., Wilms, J., et al. 2014, *ApJ*, **780**, 133
- Fürst, F., Walton, D. J., Harrison, F. A., et al. 2016, *ApJ*, **831**, L14
- Fürst, F., Kretschmar, P., Grinberg, V., et al. 2018, *XMM-Newton Workshop Proceedings*
- Ghosh, P., & Lamb, F. K. 1978, *ApJ*, **223**, L83
- Ghosh, P., & Lamb, F. K. 1979, *ApJ*, **234**, 296
- Ghosh, A., Banerjee, I., & Chakrabarti, S. K. 2018, ArXiv e-prints [arXiv:1810.08249]
- Gimenez-Garcia, A., Shenar, T., Torrejon, J. M., et al. 2016, *A&A*, **591**, A26
- Gräfener, G., Koesterke, L., & Hamann, W.-R. 2002, *A&A*, **387**, 244
- Grinberg, V., Pottschmidt, K., Böck, M., et al. 2014, *A&A*, **565**, A1
- Grinberg, V., Hell, N., El Mellah, I., et al. 2017, *A&A*, **608**, A143
- Hamann, W.-R., & Koesterke, L. 1998, *A&A*, **335**, 1003
- Hatchett, S., & McCray, R. 1977, *ApJ*, **211**, 552
- Hiltner, W. A., Werner, J., & Osmer, P. 1972, *ApJ*, **175**, L19
- Ho, C., & Arons, J. 1987, *ApJ*, **316**, 283
- Horedt, G. P. 2000, *ApJ*, **541**, 821
- Hu, C.-P., Chou, Y., Ng, C.-Y., Lin, L. C.-C., & Yen, D. C.-C. 2017, *ApJ*, **844**, 16
- Huarte-Espinosa, M., Carroll-Nellenback, J., Nordhaus, J., Frank, A., & Blackman, E. G. 2012, *MNRAS*, **433**, 295
- Illarionov, A. F., & Sunyaev, R. A. 1975, *A&A*, **39**, 00
- Israel, G. L., Belfiore, A., Stella, L., et al. 2017, *Science*, **355**, 817
- Jones, D., & Boffin, H. M. 2017, *Nat. Astron.*, **1**, 0117
- Karino, S. 2014, *PASJ*, **66**, 2
- Krticka, J., Kubat, J., & Krtickova, I. 2018, *A&A*, **620**, A150
- Lucy, L. B., & Solomon, P. M. 1970, *ApJ*, **159**, 879
- MacLeod, M., & Ramirez-Ruiz, E. 2015, *ApJ*, **803**, 41
- MacLeod, M., Antoni, A., Murgia-Berthier, A., Macias, P., & Ramirez-Ruiz, E. 2017, *ApJ*, **838**, 56
- Manousakis, A., & Walter, R. 2015, *A&A*, **58**, A58
- Manousakis, A., Walter, R., & Blondin, J. 2014, in *Phys. Magnetos. Boundary*, eds. E. Bozzo, P. Kretschmar, M. Audard, M. Falanga, & C. Ferrigno (Geneva, Switzerland), *EPJ Web Conf.*, **64**, 8205
- Martínez-Núñez, S., Kretschmar, P., Bozzo, E., et al. 2017, *Space Sci. Rev.*, **212**, 59
- Medvedev, M. V., & Narayan, R. 2000, *ApJ*, **554**, 1255
- Mohamed, S., & Podsiadlowski, P. 2007, *ASP Conf. Ser.*, **372**, 397
- Molteni, D., Tóth, G., & Kuznetsov, O. A. O. 1999, *ApJ*, **516**, 411
- Moreno Méndez, E. 2011, *MNRAS*, **413**, 183
- Moreno Méndez, E., Brown, G. E., Lee, C.-H., & Park, I. H. 2008, *ApJ*, **689**, L9
- Murgia-Berthier, A., MacLeod, M., Ramirez-Ruiz, E., Antoni, A., & Macias, P. 2017, *ApJ*, **845**, 173
- Narayan, R., Mahadevan, R., & Quataert, E. 1998, *Theory Black Hole Accretion Disk* (Cambridge Univ. Press), 36
- Orosz, J. A., McClintock, J. E., Aufdenberg, J. P., et al. 2011, *ApJ*, **742**, 84
- Owocki, S. P., & Rybicki, G. B. 1984, *ApJ*, **284**, 337
- Paczynski, B. 1977, *ApJ*, **216**, 822
- Pettersson, J. A. 1977a, *ApJ*, **214**, 550
- Pettersson, J. A. 1977b, *ApJ*, **216**, 827
- Quaintrell, H., Norton, A. J., Ash, T. D. C., et al. 2003, *A&A*, **401**, 313
- Rawls, M. L., Orosz, J. A., McClintock, J. E., et al. 2011, *ApJ*, **730**, 11
- Romano, P., Bozzo, E., Mangano, V., et al. 2015, *A&A*, **576**, L4
- Saladino, M. I., Pols, O. R., van der Helm, E., Pelupessy, I., & Zwart, S. P. 2018, *A&A*, **618**, A33
- Sana, H., de Mink, S. E., de Koter, A., et al. 2012, *Science*, **337**, 444
- Sander, A. C., Fürst, F., Kretschmar, P., et al. 2017a, *A&A*, **610**, A60
- Sander, A. C., Hamann, W.-R., Todt, H., Hainich, R., & Shenar, T. 2017b, *A&A*, **603**, A86
- Schure, K. M., Kosenko, D., Kaastra, J. S., Keppens, R., & Vink, J. 2009, *A&A*, **508**, 751
- Shakura, N., Postnov, K., Kochetkova, A., & Hjalmarsdotter, L. 2012, *MNRAS*, **420**, 216
- Shakura, N. I., Postnov, K. A., Kochetkova, A. Y., & Hjalmarsdotter, L. 2013, *Physics-Uspekhi*, **56**, 321
- Shapiro, S. L., & Lightman, A. P. 1976, *ApJ*, **204**, 555
- Smith, D. M., Heindl, W. A., & Swank, J. H. 2001, *ApJ*, **569**, 362
- Sundqvist, J. O., Owocki, S. P., & Puls, J. 2018, *A&A*, **611**, A17
- Taam, R. E., Qiao, E., Liu, B. F., & Meyer-Hofmeister, E. 2018, *ApJ*, **860**, 1
- Taani, A., Karino, S., Song, L., et al. 2019, *Res. Astron. Astrophys.*, **19**, 012
- Toro, E. F., Spruce, M., & Speares, W. 1994, *Shock Waves*, **4**, 25
- van Marle, A. J., & Keppens, R. 2011, *Comput. Fluids*, **42**, 44
- Vink, J. S., de Koter, A., & Lamers, H. J. G. L. M. 2001, *A&A*, **369**, 61
- Vreugdenhil, C. B., & Koren, B. 1993, *Numerical Methods for Advection-Diffusion Problems* (Vieweg), 373
- Walder, R., Melzani, M., Folini, D., Winisdoerfer, C., & Favre, J. M. 2014, *ASP Conf. Ser.*, **488**, 1
- Walter, R., Lutovinov, A. A., Bozzo, E., & Tsygankov, S. S. 2015, *A&ARv*, **23**, 2
- Xia, C., Teunissen, J., El Mellah, I., Chané, E., & Keppens, R. 2018, *ApJS*, **234**, 30
- Ziolkowski, J. 1985, *Acta Astron.*, **35**, 185